Modeling, Analysis, and Suppression of Demagnetization for MTPA-Driven Permanent Magnet Motors With Distributed Windings

Jinqiu Gao, Weihua Gui, *Member, IEEE*, Chao Yang, *Member, IEEE*, Tao Peng, *Member, IEEE*, Yun Yang, *Senior Member, IEEE*, Junze Luo, and Chunhua Yang, *Fellow, IEEE*

***Abstract*—This article presents novel modeling, analysis, and suppression methods for the demagnetization fault in maximum torque per ampere (MTPA) driven permanent magnet motors (PMMs) with distributed windings. First, a novel structural-mathematical technique is employed to formulate the analytical model (AM) for PMMs under a demagnetization fault. Unlike traditional AM methods, the proposed approach considers the motor structure specifically designed for the motors with distributed windings. Additionally, the new model takes the MTPA control method into account, which is well-suited for analyzing the impacts of demagnetization fault on the motor control performance. Second, a quantitative analysis of the demagnetization impacts on back electromotive force and MTPA current, based on the proposed AM, is presented. Third, to suppress demagnetization fault in MTPA-driven PMMs, a novel loss optimization-based control strategy is proposed. It utilizes predictive control principles and optimization theory to optimize losses, thus reducing the risk of demagnetization caused by temperature rise. Finally, the proposed AM and suppression strategy are validated by both finite element simulation and experiment conducted on a PMM prototype with 24 slots and 4 poles.**

***Index Terms*—Demagnetization analysis, demagnetization suppression, finite element, maximum torque per ampere (MTPA), modeling, permanent magnet motor (PMM).**

ABBREVIATIONS

PMM	Permanent magnet motor.
MTPA	Maximum torque per ampere.
PM	Permanent magnet.
FEM	Finite-element analysis.
AM	Analytical model.
HM	Hybrid model.
EMF	Electromotive force.
ACR	Automatic current control.
ASR	Automatic speed control.
MPC	Model predictive control.
FCS-MPC	Finite control set model predictive current control.
THD	Total harmonic distortion.
PI	Proportional integral.
SVPWM	Space vector pulse width modulation.
LoF	Lines of force.
AMD	Air-gap magnetic density.
$N_1, N_2, \ldots$	North pole of permanent magnet.
$S_1, S_2, \ldots$	South pole of permanent magnet.
PD	Partial demagnetization.
UD	Uniform demagnetization.
DPM	Discrete predictive model.
SPP	Slots per pole per phase.
NdFeB	Neodymium iron boron.
PC	Personal computer.

Manuscript received 22 November 2023; revised 10 March 2024; accepted 20 April 2024. Date of publication 3 May 2024; date of current version 20 June 2024. This work was supported in part by the National Natural Science Foundation of China under Grant 62233012, Grant 62173350, and Grant 62203474, and in part by the Key Laboratory of Energy Saving Control and Safety Monitoring for Rail Transportation under Grant 2017TP1002. Recommended for publication by Associate Editor R. Kennel. *(Corresponding authors: Chao Yang; Yun Yang.)*

Jinqiu Gao, Weihua Gui, Chao Yang, Tao Peng, Junze Luo, and Chunhua Yang are with the School of Automation, Central South University, Changsha 410083, China (e-mail: jinqiug@csu.edu.cn; gwh@csu.edu.cn; chaoyang@csu.edu.cn; pandtao@csu.edu.cn; 214611033@csu.edu.cn; ychh@csu.edu.cn).

Yun Yang is with the School of Electrical and Electronic Engineering, Nanyang Technological University, Singapore 639798 (e-mail: yun.yang@ntu.edu.sg).

Color versions of one or more figures in this article are available at https://doi.org/10.1109/TPEL.2024.3396466.

Digital Object Identifier 10.1109/TPEL.2024.3396466

I. INTRODUCTION

PMMS controlled by MTPA techniques are characterized by high efficiency, high power density, and low loss, making both motors and control strategies widely adopted in the fields of transportation, mining, and manufacturing, etc. [1], [2], [3]. However, there are still many challenges influencing the system performance when using PMMs, one of which is that PMs installed in the motors are prone to get demagnetized in harsh conditions such as intensive vibration, high operating temperature, or high flux-weakening current during wide-range speed regulation [4], [5]. Considering that PM demagnetization can significantly reduce motor efficiency and torque output, it is crucial to analyze its mechanisms and impacts [6], [7], and to subsequently formulate effective strategies for mitigating demagnetization faults.

Many up-to-date studies on PM demagnetization faults have been carried out, covering five key areas [8], [9], [10], [11]: motor modeling under fault; analysis of PM demagnetization impacts; fault diagnosis [12]; fault handling [13]; and fault suppression. First, modeling is the cornerstone of PM demagnetization research. It is crucial for analyzing the performance of faulty motors and developing model-based fault diagnosis strategies [14].

Effective modeling is indispensable for initiating and advancing relevant research. Second, analysis plays a fundamental role in revealing the nature and impact of faults [15]. It significantly enhances our comprehension of how faults affect operational performance and safety, thus motivating researchers to propose strategies for fault handling and suppression. Third, many scholars have been dedicated to formulating efficient techniques for the detection of demagnetization faults. These methodologies can be classified into three principal categories: the magnetic characteristic analysis method; the electrical signature analysis method; and the mechanical analysis method [16]. Fourth, fault handling refers to how to ensure that the motor can still operate efficiently after the fault occurs, which is a postfault handling measure. Common methods include adaptive control [17] and flux-intensifying control techniques [18]. Finally, the goal of fault suppression is to stop the undesirable demagnetization from occurring in the first place or lessen the severity of the fault [19]. Employing effective fault suppressing strategies offers many benefits, including improved system reliability, reduced maintenance costs, and more. Notably, proactive mitigation of faults could significantly lessen the immediate need for additional research in this area. Among these aspects, it is worth noting that modeling, analysis, and fault suppression have a more direct impact on understanding and mitigating faults compared to fault diagnosis and handling, thereby requiring further investigation.

The traditional models of PMMs under the demagnetization fault include FEM, AM, and HM [8], [11], [17], [18], [19], [20], [21]. The FEM is well-known for its high accuracy, capturing each detail within the motor. For instance, Zhu et al. [8] present an FEM with specific considerations of the silicon steel oversaturation and irreversible PM demagnetization. However, FEM's requirement for substantial memory and longer computation times limits its practicality in certain scenarios. Farooq et al. [11], Gui et al. [17], and Wang et al. [18] introduce different magnetic equivalent circuit-based AMs developed through methods of direct deduction and solving Maxwell's magnetic equations. AM, grounded in the electric motor theory, constructs the magnetic field information of PMs and offers faster computational speeds. The HM, which integrates FEM and AM, leverages the strengths of both modeling methods [19], [20]. But it still requires precise motor structural data, often not readily available to users. Comparatively, AMs present significant advantages in terms of computational burden and data accessibility compared to the other models. Despite these advancements, current research presents limitations. Practical applications feature diverse motor structures, such as different winding types (e.g., distributed and centralized windings), which previous studies have often overlooked [21]. For different motor structures, the model of the motor under demagnetization fault should be different. However, most existing studies focus on the universal PMMs, neglecting these structural variations. These factors lead to model inaccuracy, which deserves further investigation. Finally, all AMs do not take control methods into account. This is not conducive to subsequent research in fault analysis and handling.

Current fault analysis mainly focuses on the impact of demagnetization on performance aspects, including back EMF, harmonics, vibration, noise, and others [22], [23], [24], [25], [26]. For example, Usman et al. [27] investigates the relationship between PM demagnetization and various factors such as the magnetic flux, stator current, back EMF, electromagnetic torque, vibration and noise. Contrastive analysis reveals that variations in the magnetic field distribution contribute to the degradation of electrical and mechanical performance. A limitation of traditional analysis methods is their tendency to treat PMMs as generators. And the analytical results are often qualitative, such as PM demagnetization increasing stator current. However, few studies focus on quantitative analysis, determining the extent of current increase relative to a specific demagnetization ratio. This gap exists because quantitative analysis is more complex, necessitating the treatment of PMMs as motors rather than generators and requiring the incorporation of control methods.

At present, most strategies aimed at suppressing demagnetization focus on advancements in motor structural design and improvements in the PM materials [28], [29], [30]. For example, Jung et al. [28] demonstrates that optimizing the core shape reduces eddy current loss in the motor's PM, effectively controlling rotor temperature and, thereby, suppressing irreversible demagnetization. Similarly, Farrok et al. [29] introduces a novel design for the PM linear generator's translator, employing a variable length of air gap topology to counteract demagnetization. However, there is a lack of literatures at the control strategies to suppress demagnetization for PMMs.

To solve the aforesaid issues, this article conducts a comprehensive study on demagnetization faults in MTPA-driven PMMs with distributed windings, encompassing aspects of modeling, analysis, and suppression. The main novelties and contributions are summarized as follows.

1) An innovative structural-mathematical technique is proposed to establish a general AM of PMMs under demagnetization faults. This model represents an advancement over traditional AM methods, as it is specifically tailored for motors with distributed windings and addresses the impact of motor structure on modeling accuracy. Furthermore, when establishing the model of the PMMs, rather than treating them solely as generators, the approach takes on the theory from a motor perspective and incorporates the motor control method, that is, MTPA control technique.
2) Utilizing the proposed general AM and with control strategy considered, this article achieves quantitative analysis of the demagnetization impacts on the back EMF of a specific PMM. Subsequently, the extent to which MTPA current motor increase is derived. By delving into the analysis of demagnetization faults, more convincing conclusions are drawn regarding the necessity of suppressing faults in practical applications. This contributes to the enrichment of existing PM demagnetization fault analysis theories and the enhancement of understanding of the fault.
3) For the MTPA-controlled PMMs, a suppression method based on loss optimization is proposed, which addresses the factors that could lead to demagnetization faults due to increased temperature. Unlike strategies based on motor structural design, this method focuses on control and optimization. Specifically, an optimized MTPA control

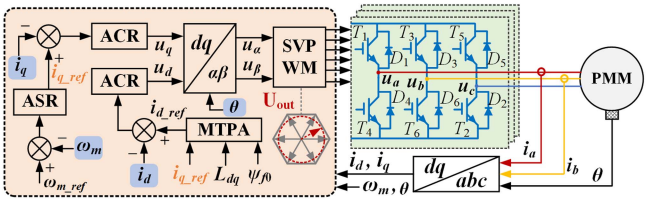

i_{d_ref}, i_{q_ref}: d, q-axis reference currents , $u_{\alpha,\beta}$: α, β-axis voltages, ω_{m_ref}: reference speed , $\mathbf{U_{out}}$: output voltage, $T_{1,2,3,4,5,6}$, $D_{1,2,3,4,5,6}$: power devices,

Fig. 1. MTPA-driven permanent magnet motor drive.

strategy is developed. It begins with loss prediction, utilizes predictive control principles, and employs optimization theory to establish a cost function to evaluate the magnitude of losses. This method can generate effective control variables for reducing motor losses and mitigating temperature increases.

The rest of this article is organized as follows. Section II constructs the general AM of MTPA-driven PMMs with distributed windings. Section III presents the impacts of demagnetization. To clearly illustrate the conclusions drawn from Section II and make it easy for readers to understand the necessity of developing demagnetization fault suppression methods, a specific motor is adopted for quantitative analysis. In Section IV, a suppression method based on loss optimization is proposed, which is applicable to general PMMs. In Section V, the general AM, analytical results and the proposed demagnetization suppression control method are verified by experimental results. Finally, Section VI concludes this article.

II. AMs of PMMs With Distributed Windings

As for the structures of MTPA-driven PMMs shown in Fig. 1, when taking the flux linkage inside the motor as the intermediate variables and ignoring magnetic saturation, eddy current and hysteresis loss, the machine model in the *abc*-axis reference frame can be described as

$$\begin{cases} u_a = i_a R_s + \frac{d\psi_a}{dt} + \frac{d\psi_f \cos\theta}{dt} \\ u_b = i_b R_s + \frac{d\psi_b}{dt} + \frac{d\psi_f \cos(\theta - 2\pi/3)}{dt} \\ u_c = i_c R_s + \frac{d\psi_c}{dt} + \frac{d\psi_f \cos(\theta - 4\pi/3)}{dt} \end{cases} \tag{1}$$

where i_a, i_b, and i_c are a, b, c-phase currents. u_a, u_b, and u_c are a, b, c-phase voltages. R_s is stator resistance. θ is electrical position (rotating angle), ψ_f is overall flux linkage generated by the PMs and it is a constant. ψ_a, ψ_b, and ψ_c are flux linkage generated by stator windings and they can be represented as

$$\begin{bmatrix} \psi_a \\ \psi_b \\ \psi_c \end{bmatrix} = \begin{bmatrix} L_{aa} & M_{ab} & M_{ac} \\ M_{ba} & L_{bb} & M_{bc} \\ M_{ca} & M_{cb} & L_{cc} \end{bmatrix} \begin{bmatrix} i_a \\ i_b \\ i_c \end{bmatrix} \tag{2}$$

where L_{aa}, L_{bb}, and L_{cc} are the self-inductances of the stator windings. M_{ab}, M_{ba}, M_{ac}, M_{ca}, M_{bc}, and M_{cb} are the mutual inductances of the stator windings. For the sake of clearness, taking the a-phase winding that has similar properties to the other two phases (except phase angles) as an example, (1) can

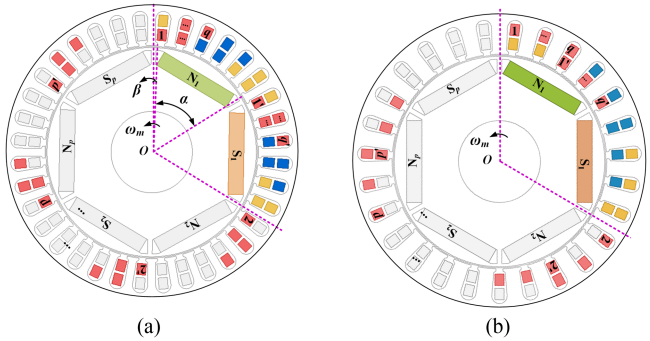

(a) (b)

Fig. 2. General PMM Structure designed with disturbed windings and integer slot. (a) Integer-pitch PMM. (b) Fraction-pitch PMM.

be further derived as

$$u_a = i_a R_s \underbrace{+\frac{\mathrm{d}\psi_a}{\mathrm{d}t}}_{\text{Induced back-EMF}} \underbrace{-p\omega_m \psi_f \sin\theta}_{\text{Motional back-EMF}} \tag{3}$$

where p is the number of pole pairs. ω_m is rotor mechanical angular speed. Based on the Faraday's law of electromagnetic induction, the motional back electromotive force (EMF) in (3) can also be described as the back EMF generated when the conductors of windings cut through the LoF. The derivations concerning the a-phase windings are detailed as follows.

As for the PM motor with distributed windings, its features include that a-phase occupies s/m slots, where m is the number of motor phases, and the number of slots per pole per phase is $s/2mp$, where s is the total number of slots. With reference to Fig. 2, denote analysis AMD at which the s/m a-phase slots are located as $B_{\theta i}$ and $B_{\theta i'}$, respectively, where i represents the ith coil. $B_{\theta i}$ and $B_{\theta i'}$ are associated with the leading and lagging slots for each coil with the speed direction considered, respectively. Then, motional back EMF M_{EMF} can be calculated by

$$\begin{aligned} M_{\mathrm{EMF}} &= \sum_{i=1}^{zs/2m} (B_{\theta i} - B_{\theta i'}) N_c l v \\ &\approx \sum_{i=1}^{zs/2m} (B_{\theta i} - B_{\theta i'}) N_c l \omega_m \frac{d}{2} \end{aligned} \tag{4}$$

where N_c is the number of a-phase conductors in per slot per layer. l is the equivalent length of one conductor. v is the linear speed where the conductors cut through LoF. d is the inner diameter of stator. z is the number of the motor winding layers.

In this section, the research focus has shifted from the analysis of a specific motor instance to the broader domain of PMMs. The primary objective of this section lies in the exploration of the universal applicability of PMMs, with the intent to provide both theoretical foundations across a diverse spectrum of application scenarios. This comprehensive analysis is then contrasted with findings derived from the specific motor instance, thereby revealing overarching principles.

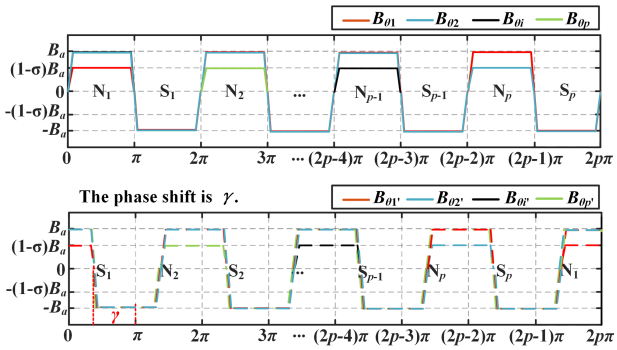

Fig. 3. Air-gap magnetic density property when one permanent (N) encounters demagnetization fault.

Define the number of virtual slots (q) covered by per pole per phase as

$$q = \frac{zs}{2pm}. \tag{5}$$

Due to the characteristics of a motor with distributed windings, the magnetic potential and back EMF in each phase of the motor is generated through the combined superposition of conductors distributed across multiple slots. When a motor with distributed winding and integer-q, the stator windings are uniformly distributed within the machine, ensuring a fixed number of slots per phase corresponding to each PM pair pole. This kind of motor structure is shown in Fig. 2. When $s/2pm$ is an integer number, the motor is an integer-pitch motor as Fig. 2(a). Otherwise, it is a fractional-pitch motor as Fig. 2(b). Therefore, it is possible to analyze the conductors within one slot under one of the magnetic poles, which correspondingly obtains the back EMF of the conductors within that slot position under each magnetic pole.

After substituting (4) into (3), a new machine model can be obtained as

$$u_a = i_a R_s + \frac{d\psi_a}{dt} + \sum_{j=1}^{q}\sum_{i=1}^{p}(B_{\theta i} - B_{\theta i'})N_c l\omega_m \frac{d}{2}. \tag{6}$$

Now, as long as $B_{\theta i}$ and $B_{\theta i'}$ are obtained, (6) can be used to analyze the PM motor under different magnetic situations. When the motor works, the variation trend of the AMD at a particular point such as $B_{\theta 1}$ is closely related to the rotor position θ. Specifically, it complies with the distribution curve of the AMD generated by the PMs of a motor, of which shape is similar to the *B-curve* (e.g., B_0 and B_θ at different positions) in Fig. 3. It deserves to be mentioned that the distribution curve of the AMD is not sinusoidal inside the PM motor, and instead, it is trapezoidal due to the distribution of the PMs when the cogging effect is ignored. While in the area a PM can cover, the AMD remains constant, of which magnitude can be calculated by (7) when leakage flux is ignored

$$\begin{cases} B_a = \frac{2B_r l_{\mathrm{PM}} l}{\alpha d l} = \frac{2B_r l_{\mathrm{PM}}}{\alpha d} \\ B_{a\_d} = (1-\sigma)B_a, 0 \le \sigma \le 1 \end{cases} \tag{7}$$

where B_r is PM remanence, α is the angle that a PM can cover, l_{PM} is width of the PM, σ is demagnetization degree, B_a and B_{a_d} are the magnitudes of AMD generated by the healthy and postfault PMs, respectively.

$2p$ partial back EMF is assessed since there are $2p$ regions according to the number of poles. The resultant back EMF is a piecewise function composed by each piece of partial back EMF according to the rotor position [31]. According to the AMD property of the health motor in Fig. 3, the AMD of the PMM with distributed winding and integer-q can be written as

$$F_B(\theta) = \begin{cases} \frac{B_a}{\beta}\theta, if 0 + k\pi \le \theta < \beta + k\pi \\ B_a, if \beta + k\pi \le \theta < (\pi - \beta) + k\pi \\ -\frac{B_a}{\beta}(\theta - \pi), if (\pi - \beta) + k\pi \le \theta < \pi + k\pi \end{cases}$$

$$\beta = \frac{\pi - \alpha}{2} \tag{8}$$

$$\begin{aligned} B_{\theta 1}(\theta) &= \begin{cases} F_B(\theta), if 0 + 2kp\pi \le \theta < \pi + 2kp\pi \\ -F_B(\theta), if \pi + 2kp\pi \le \theta < 2\pi + 2kp\pi \\ \cdots \\ F_B(\theta), if (2p-1)\pi + 2kp\pi \le \theta < 2p\pi + 2kp\pi \end{cases} \\ &= (-1)^{i-1}F_B(\theta), if (i-1)\pi + 2kp\pi \\ &\qquad \le \theta < i\pi + 2kp\pi \\ i &= 1, 2, \ldots, 2p \end{aligned} \tag{9}$$

where i is positive integer and β is the angle that a PM cannot cover which is fixed by the motor structure.

The magnetic properties of UD is fundamentally consistent with the healthy motor discussed earlier. When the UD occurs, all magnetic poles would demagnetize symmetrically. Hence, this section will further focus on modeling the PD fault PMMs. This article specifically investigates PD faults caused by the demagnetization of an entire magnetic pole. Other forms of local demagnetization are not covered in this article. During analysis, magnetic saturation is ignored because it contributes less to the main objective of this article, which is to propose a modeling method capable of analyzing and quantitatively assessing the impact of demagnetization faults. Besides, the approximation is made that during PD fault, only changes in the demagnetized poles are considered, while variations in the other poles are ignored. Assuming that the first north magnetic pole N_1 is demagnetized, (9) can be modified as

$$\begin{aligned} B_{\theta 1\mathrm{PD}}(\theta) &= \begin{cases} (1-\sigma)F_B(\theta), if 0 + 2kp\pi \le \theta < \pi + 2kp\pi \\ -F_B(\theta), if \pi + 2kp\pi \le \theta < 2\pi + 2kp\pi \\ \cdots \\ F_B(\theta), if (2p-1)\pi + 2kp\pi \\ \le \theta < 2p\pi + 2kp\pi \end{cases} \\ &= \begin{cases} (1-\sigma)F_B(\theta), if 0 + 2kp\pi \le \theta < \pi + 2kp\pi \\ (-1)^{j-1}F_B(\theta), if (j-1)\pi + 2kp\pi \\ \le \theta < j\pi + 2kp\pi \end{cases} \\ j &= 2, 3, \ldots, 2p. \end{aligned} \tag{10}$$

In order to express the analytical formula of the motor's back EMF more clearly, priority is given to considering the magnetic

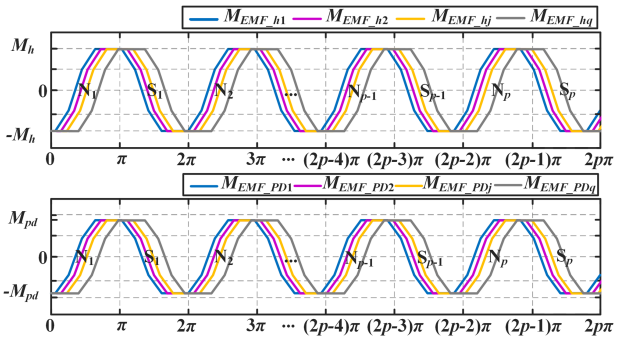

Fig. 4. Whole back EMF of the conductors in each pole pair under the PMM with one north pole demagnetization fault.

flux expression of slots in the same position under different magnetic poles. In Fig. 2, in the motor's forward rotation direction, slots at the same position under the *N*-pole are sequentially labeled as 1, 2, …, *p*, while those under the *S*-pole are labeled as 1', 2', …, *p*' in corresponding order. These AMD of different slots can be obtained by

$$B_{\theta i}(\theta) = B_{\theta 1}(\theta - 2(i-1)\pi) \tag{11}$$

$$B_{\theta i'}(\theta) = B_{\theta i}(\theta - \pi + \gamma) \tag{12}$$

where γ is the phase shift. The value of γ depends on the specific design of the motor winding. The γ of the integer-pitch PMM is zero.

When the first north magnetic pole is demagnetized, the AMD of different slots under demagnetization fault exhibit periodic variations. These can be described as

$$B_{\theta i\mathrm{PD}}(\theta) = \begin{cases} (1-\sigma)F_B(\theta) \\ if 2(p-i+1)\pi + 2kp\pi \\ \le \theta < 2(p-i+1)\pi + \pi + 2kp\pi \\ (-1)^{j-1}F_B(\theta) \\ if (j-1)\pi + 2kp\pi \le \theta < j\pi + 2kp\pi, \\ j \ne 2(p-i+1)+1 \end{cases} \tag{13}$$

$$B_{\theta i'\mathrm{PD}}(\theta) = \begin{cases} (1-\sigma)F_B(\theta), \\ if 2(p-i)\pi + 3\pi - \gamma + 2kp\pi \\ \le \theta < 2(p-i)\pi + 4\pi - \gamma + 2kp\pi \\ (-1)^{j}F_B(\theta), \\ if (j-1)\pi - \gamma + 2kp\pi \le \theta < j\pi - \gamma \\ +2kp\pi, j \ne 2(p-i+1)+2 \end{cases} . \tag{14}$$

Through the analysis of AMD, we can further obtain the equation for the motor's back EMF by (4). From the Fig. 4, it can be observed that both B_θ and $B_{\theta'}$ experience a decrease in magnetic flux density in each positive half-cycle due to the presence of the N_1 pole. In this context, $B_{\theta'}$, due to the opposite direction of the conductor current in the slot compared to the current under B_θ, requires a negative sign when synthesizing the back EMF. As a result, $-B_{\theta'}$ exhibits a decrease in magnetic flux density in each negative half-cycle. Therefore, in the presence of PD fault, the synthesized back EMF of conductors at the same position in each phase and each pole pair uniformly decreases during both the positive and negative half-cycles, as opposed to healthy machines where only amplitude variations are present in the synthesized back EMF. So, the fixed single-slot (per phase per pole) conductors' motional back EMF of a healthy PMM (M_{EMF_h1}) and a PD PMM (M_{EMF_PD1}) can be calculated as

$$M_{\mathrm{EMF}\_h1} = \sum_{i=1}^{p}(B_{\theta i} - B_{\theta i'})N_c l\omega_m \frac{d}{2} \tag{15}$$

$$\begin{aligned} M_{\mathrm{EMF\_PD1}} &= \sum_{i=1}^{p}(B_{\theta i\mathrm{PD}} - B_{\theta i'\mathrm{PD}})N_c l\omega_m \frac{d}{2} \\ &= \frac{2p-\sigma}{2p}M_{\mathrm{EMF}\_h1}. \end{aligned} \tag{16}$$

As illustrated in Fig. 4, summing up the back EMF of the conductors in different slot (1, 2, …, *p*) under each pole pair for each phase, we obtain the analytical expression for the total back EMF of one phase of the motor (M_{EMF_ha}) as follows

$$\begin{aligned} M_{\mathrm{EMF}\_ha} &= M_{\mathrm{EMF}\_h1}(\theta) + M_{\mathrm{EMF}\_h2}(\theta) + \ldots + M_{\mathrm{EMF}\_hq}(\theta) \\ &= M_{\mathrm{EMF}\_h1}(\theta) + M_{\mathrm{EMF}\_h1}\left(\theta + k_1\frac{2p\pi}{s}\right) + \ldots \\ &\quad + M_{\mathrm{EMF}\_h1}\left(\theta + k_{q-1}\frac{2p\pi}{s}\right). \end{aligned} \tag{17}$$

Similarly the total back EMF ($M_{\mathrm{EMF\cdot PD}\,a}$)of one phase of the PMM under the PD fault can be described as

$$\begin{aligned} M_{\mathrm{EMF\_PD}a} &= M_{\mathrm{EMF\_PD1}}(\theta) + M_{\mathrm{EMF\_PD2}}(\theta) \\ &\quad + \ldots + M_{\mathrm{EMF\_PD}q}(\theta) \\ &= M_{\mathrm{EMF\_PD1}}(\theta) + M_{\mathrm{EMF\_PD1}}\left(\theta + k_1\frac{2p\pi}{s}\right) \\ &\quad + \ldots + M_{\mathrm{EMF\_PD1}}\left(\theta + k_{q-1}\frac{2p\pi}{s}\right) \\ &= \frac{2p-\sigma}{2p}M_{\mathrm{EMF}\_ha}. \end{aligned} \tag{18}$$

From (18), it can be observed intuitively that the PMM with distributed winding and integer-q motion back EMF only undergoes changes in amplitude when PD faults occur, without exhibiting any harmonic variations. It should be noted that the analysis process and results outlined above require that the motors have distributed windings. Furthermore, the value of q in (5) should be an integer. Table I gives the suitable applications for the number of SPP. It can be observed that the value of motor

TABLE I
SUITABLE APPLICATIONS FOR THE NUMBER OF SLOTS PER POLE PER PHASE

Winding layers	1					2				
SPP	1/4	1/3	1/2	1	2	1/4	1/3	1/2	1	2
Suitability	X	X	X	√	√	X	X	√	√	√

TABLE II
MOTOR PROTOTYPE PARAMETERS

Parameter	VALUE	Unit
number of slots s	24	-
number of pole pairs p	2	-
conductor number in one slot N_c	69	-
length of conductor l	0.1	m
inner diameter of stator d	0.08	m
thickness of PM h_{PM}	3.5	mm
PM-covering angle α	5π/12	rad
PM remanence B_r	0.95	T
d-axis inductance L_d	28.2	mH
q-axis inductance L_q	62.63	mH
phase resistance R_s	1.469	Ω
rated load T_l	4	Nm

winding layers influences the suitability in applications with nonfractional number of slots. When it comes to the fractional number of slots, the proposed method is well-suited.

On the one hand, by substituting the back EMF into the MTPA-driven PMM (3), it can be deduced that due to the decrease in magnetic flux amplitude, the back EMF experiences amplitude changes. On the other hand, the AM reveals that demagnetization in PMMs with distributed winding does not significantly change the harmonics and phase angle of back EMF. Considering that the back EMF properties are closely related to the motor current harmonics, the current harmonics do not undergo noticeable changes either. These happen because the magnetic saturation issue is ignored.

III. IMPACTS OF DEMAGNETIZATION FAULT ON MTPA-DRIVEN PMMS

This section uses the AM established in Section II to analyze the impacts of demagnetization fault on the performance (back EMF and currents) of MTPA-driven motors quantitatively. For the sake of clarity, take a PMM prototype with distributed windings (see Fig. 5) as an example for analysis. The parameters of the motor is given in Table II.

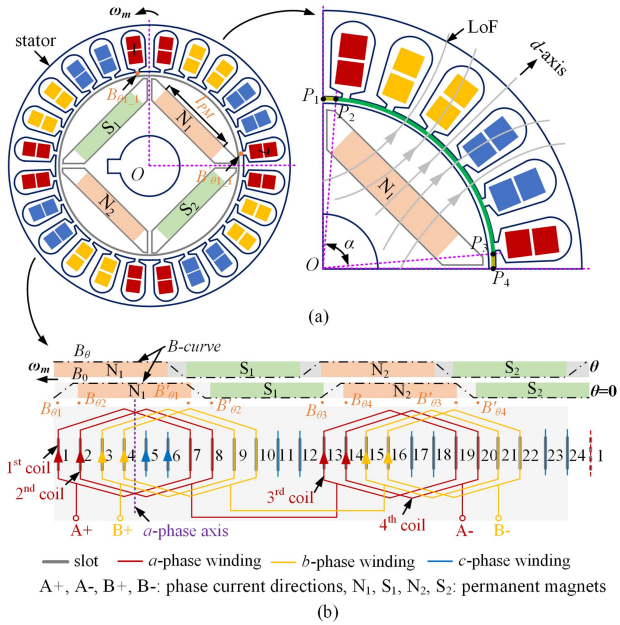

Fig. 5. Structure of specific permanent magnet motor prototype with 24 slots and 4 poles. (a) Overall structure. (b) Outspread diagram.

A. Impacts of Demagnetization Fault on Back EMF

To intuitively explain the AM model, a PMM prototype with 24 slots ($s = 24$), 4 poles ($p = 2$) and distributed winding shown Fig. 5 is formulated as an example. First, the a-phase winding has $s/6 = 4$ coils, occupying a total of $s/3 = 8$ slots (1, 2, 7, 8, 13, 14, 19, and 20), and the number of slots per pole per phase is $s/6p = 2$. The winding pitch is $s/2p = 6$. The number of q is $zs/2mp = 2$. Denote the AMD at the positions corresponding to the four coils (eight slots) as $B_{\theta 1}$, $B_{\theta 2}$, $B_{\theta 1'}$, $B_{\theta 2'}$, $B_{\theta 3}$, $B_{\theta 4}$, $B_{\theta 3'}$, and $B_{\theta 4'}$, respectively. With the speed direction considered, slot 1 is ahead of slot 7 for the first coil, so the sign of $B_{\theta 1}$ is positive while $B_{\theta 1'}$ is negative in (5). This also applies to the other three coils. On this ground, since the conductors in each slot interact with $B_{\theta 1}, B_{\theta 2}, \ldots$ and $B_{\theta 4'}$ when the rotor reaches θ, respectively, the

$$B_{\theta 1}(\theta) = \begin{cases} \frac{2B_a}{\pi - p\alpha}\left(\theta - \frac{(s-6p)\pi}{6s} - 2k\pi\right), \text{if } \frac{3ps\alpha-(2s+6p)\pi}{6s} + 2k\pi \le \theta < \frac{(4s-6p)\pi-3ps\alpha}{6s} + 2k\pi \\ B_a, \text{if } \frac{(4s-6p)\pi-3ps\alpha}{6s} + 2k\pi \le \theta < \frac{(4s-6p)\pi+3ps\alpha}{6s} + 2k\pi \\ \frac{2B_a}{p\alpha-\pi}\left(\theta - \frac{(10s-6p)\pi-3ps\alpha}{6s} - 2k\pi\right) - B_a, \text{if } \frac{(4s-6p)\pi+3ps\alpha}{6s} + 2k\pi \le \theta < \frac{(10s-6p)\pi-3ps\alpha}{6s} + 2k\pi \\ -B_a, \text{if } \frac{(10s-6p)\pi-3ps\alpha}{6s} + 2k\pi \le \theta < 2(k+1)\pi \& 2k\pi \le \theta < \frac{3ps\alpha-(2s+6p)\pi}{6s} + 2k\pi \end{cases} \tag{19}$$

$$B_{\theta 1}(\theta) = \begin{cases} \frac{(B_a+B_{a\_d})}{\pi - p\alpha}\left(\theta + \frac{(6p+2s)\pi-3ps\alpha}{6s}\right) - B_a, if \frac{3ps\alpha-(2s+6p)\pi}{6s} \le \theta < \frac{(4s-6p)\pi-3ps\alpha}{6s} \\ B_{a\_d}, if \frac{(4s-6p)\pi-3ps\alpha}{6s} \le \theta < \frac{(4s-6p)\pi+3ps\alpha}{6s} \\ \frac{(B_a+B_{a\_d})}{p\alpha-\pi}\left(\theta - \frac{(10s-6p)\pi-3ps\alpha}{6s}\right) - B_a, \text{if } \frac{(4s-6p)\pi+3ps\alpha}{6s} \le \theta < \frac{(10s-6p)\pi-3ps\alpha}{6s} \\ -B_a, \text{if } \frac{(10s-6p)\pi-3ps\alpha}{6s} + 2k\pi \le t < 2(k+1)\pi \text{and} 2k\pi \le \theta < \frac{3ps\alpha-(2s+6p)\pi}{6s} + 2k\pi, k = 0, 1, 2, \ldots, p-1 \\ \frac{2B_a}{\pi - p\alpha}\left(\theta - \frac{(s-6p)\pi}{6s} - 2k\pi\right), \text{if } \frac{3ps\alpha-(2s+6p)\pi}{6s} + 2k\pi \le \theta < \frac{(4s-6p)\pi-3ps\alpha}{6s} + 2k\pi, k = 1, 2, \ldots, p-1 \\ B_a, \text{if } \frac{(4s-6p)\pi-3ps\alpha}{6s} + 2k\pi \le \theta < \frac{(4s-6p)\pi+3ps\alpha}{6s} + 2k\pi, k = 1, 2, \ldots, p-1 \\ \frac{2B_a}{p\alpha-\pi}\left(\theta - \frac{(10s-6p)\pi-3ps\alpha}{6s} - 2k\pi\right) - B_a, \text{if } \frac{(4s-6p)\pi+3ps\alpha}{6s} + 2k\pi \le \theta < \frac{(10s-6p)\pi-3ps\alpha}{6s} + 2k\pi, k = 1, 2, \ldots, p-1 \end{cases} \tag{20}$$

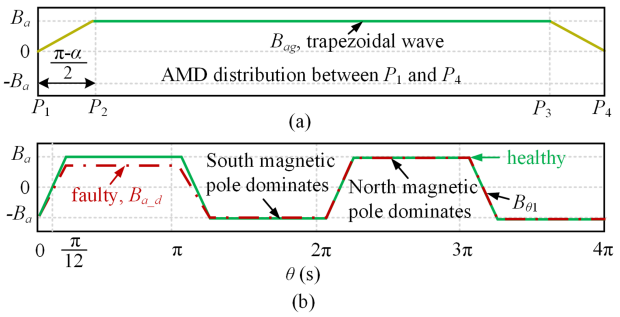

Fig. 6. Air-gap magnetic density property. (a) Distribution diagram between P_1 and P_4 when the rotor position is zero. (b) Variation trend of $B_{\theta 1}$ when rotor makes one revolution from zero position.

one-slot motional back EMF can be calculated by $NB_{\theta i}l\omega_m d/2$ or $-NB_{\theta i'}l\omega_m d/2$, and M_{EMF} equals the sum of them. Then, because $B_{\theta 1}$, $B_{\theta 2}$, $B_{\theta 3}$ and $B_{\theta 4}$ are dominated by the north magnetic pole (LoF radiates outward from shaft) obviously, their values are positive based on (4), while the others are negative. Finally, before leaving Fig. 2(b), it deserves to be mentioned that when θ is zero, at which the a-phase axis complies with one north magnetic pole, M_{EMF} gets to zero because $B_{\theta i} = B_{\theta i'}$. When a healthy motor spins from 0 to $2p\pi$, with reference to Fig. 6, the variation trend of the AMD at $B_{\theta 1}$ can be described as (19) shown att the bottom of the previous page, considering symmetry.

On the one hand, if the UD occurs, all the PMs are demagnetized uniformly. The symmetry of magnetic field (magnetic symmetry) is not influenced. In this case, (19) is still suitable for describing the AMD property at $B_{\theta 1}$ when B_{a_d} (instead of B_a) is adopted. On the other hand, when PD fault occurs. As shown in Fig. 6(b), the magnetic symmetry is damaged. Assuming that a north magnetic pole is demagnetized, (19) can be modified as (20) shown att the bottom of the previous page, which becomes totally different.

In terms of $B_{\theta i}$, it can be obtained by

$$B_{\theta i}(\theta) = \begin{cases} B_{\theta 1}\left(\theta - \frac{2p\lambda_2\pi}{s} - 2\lambda_1\pi\right) \\ \lambda_1 = \mathrm{quot}\left(i-1, \frac{s}{6p}\right), \lambda_2 = \mathrm{mod}\left(i-1, \frac{s}{6p}\right) \end{cases} \tag{21}$$

where quot () and mod () are the functions calculating quotient λ_1 and remainder λ_2, respectively. Then, $B_{\theta i'}$ is as follows

$$B_{\theta i'}(\theta) = B_{\theta i}(\theta - \pi). \tag{22}$$

After substituting the slot number ($s = 24$), pole pair number ($p = 2$) and PM-covering angle ($\alpha = 5\pi/12$) of the targeting motor into (8), (10), and (11), the motional back EMF of a healthy PMM ($M_{\mathrm{EMF\_}h}$) between 0 and 2π can be calculated by (5) as

$$M_{\mathrm{EMF\_}h} = \begin{cases} \frac{4B_aN_cl\omega_m d}{\pi}(6\theta - \pi), \mathrm{if} 0 \le \theta < \frac{\pi}{3} \\ 4B_aN_cl\omega_m d, if \frac{\pi}{3} \le \theta < \pi \\ -\frac{4B_aN_cl\omega_m d}{\pi}(6\theta - 7\pi), \mathrm{if}\pi \le \theta < \frac{4\pi}{3} \\ -4B_aN_cl\omega_m d, if \frac{4\pi}{3} \le \theta < 2\pi \end{cases}. \tag{23}$$

It should be addressed as shown in Fig. 5, between 0 and 2π, N_1, S_1 and N_2, S_2 are linked with the first, second coil, and third and fourth coils for the motor with distributed windings, respectively. When a new electrical cycle starts, although N_2 and S_2 are linked with the first and second coils while N_1 and S_1 are linked with the third and fourth ones, the variation trend of the motional back EMF between 2π and 4π is the same as that between 0 and 2π due to mechanical symmetry. Hence, the motor characteristics within one electrical cycle (0–2π) are representative for analysis.

1) UD Fault: When the UD occurs, B_a in (23) should be replaced by B_{a_d}. Considering that B_a is a factor in each equation of (23), the relation of the motional back EMF under the UD fault ($M_{\mathrm{EMF\_UD}}$) and the demagnetization degree can be described as

$$M_{\mathrm{EMF\_UD}} = (1-\sigma)M_{\mathrm{EMF\_}h}. \tag{24}$$

As for the harmonics, the proportion of each order remains unchanged in comparison with the ones of a healthy motor because the motional back EMF experiences a proportional drop.

2) PD Fault: Substitute the motor parameters into (20)–(22), and then the obtained result can be adopted to calculate the motional back EMF of the motor under the PD fault ($M_{\mathrm{EMF\_PD}}$), which can be represented as

$$M_{\mathrm{EMF\_PD}} = \begin{cases} \frac{(4-\sigma)B_aN_cl\omega_m d}{\pi}(6\theta - \pi), \mathrm{if} 0 \le \theta < \frac{\pi}{3} \\ (4-\sigma)B_aN_cl\omega_m d, \mathrm{if}\frac{\pi}{3} \le \theta < \pi \\ -\frac{(4-\sigma)B_aN_cl\omega_m d}{\pi}(6\theta - 7\pi), \mathrm{if}\pi \le \theta < \frac{4\pi}{3} \\ -(4-\sigma)B_aN_cl\omega_m d, \mathrm{if}\frac{4\pi}{3} \le \theta < 2\pi \end{cases}. \tag{25}$$

By comparing (23) and (25), it can be seen that the relationship between $M_{\mathrm{EMF\_PD}}$ and $M_{\mathrm{EMF\_}h}$ is as follows

$$M_{\mathrm{EMF\_PD}} = \left(1 - \frac{\sigma}{4}\right) M_{\mathrm{EMF\_}h}. \tag{26}$$

Interestingly, being similar to the UD fault, the motional back EMF proportionally decreases when the PD fault occurs. Intuitively speaking, the demagnetized PM only cause back EMF reduction in its linked coils, but for the other coils, the motional back EMFs are consistent with those when the motor is healthy.

B. Impacts of Demagnetization Fault on Currents

The in-depth analysis of how demagnetization impacts the current of MTPA-driven PMMs. This is detailed in this part, which serves as the crucial bridge between the theoretical groundwork laid above and its practical implications.

For the sake of simplicity, transform (1) into the dq-axis model by means of coordinate transformation technique

$$\begin{cases} \frac{di_d}{dt} = -\frac{R_s}{L_d}i_d + \frac{L_q}{L_d}p\omega_m i_q + \frac{u_d}{L_d} \\ \frac{di_q}{dt} = -\frac{L_d}{L_q}p\omega_m i_d - \frac{R_s}{L_q}i_q + \frac{u_q}{L_q} - \frac{\psi_f}{L_q}p\omega_m \\ T_e = 1.5p(\psi_f i_q + (L_d - L_q)i_d i_q) \end{cases} \tag{27}$$

where i_d, i_q, are stator dq-axis currents, u_d, and u_q are dq-axis control voltages, L_d and L_q, are dq-axis inductances. T_e is are electromagnetic torque. When using the MTPA strategy for control, the d-axis current tracks the reference one i_{d_ref} should

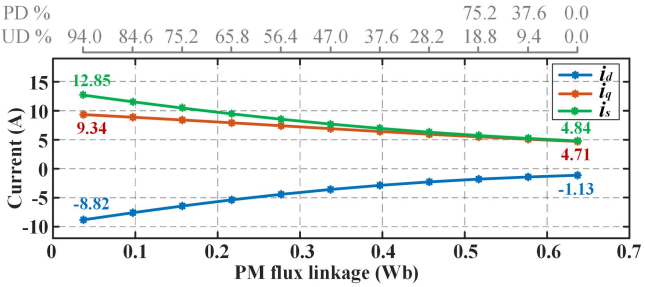

Fig. 7. Relation of motor currents versus PM flux linkage and different demagnetization degrees.

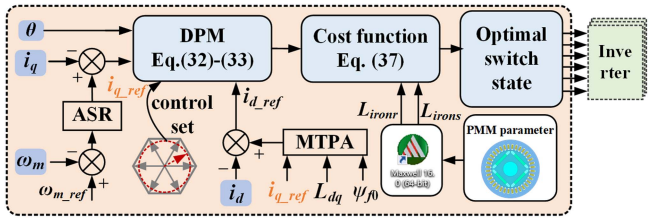

Fig. 8. MTPA-driven permanent magnet motor drive.

be set as

$$i_d = i_{d\_\mathrm{ref}} = -\frac{\psi_f}{2(L_d - L_q)} - \sqrt{\frac{{\psi_f}^2}{4(L_d - L_q)^2} + {i_q}^2}. \quad (28)$$

When the motor runs stably at a constant speed for a long time, T_e equals the load torque T_l when ignoring friction, that is,

$$T_e = T_l. \quad (29)$$

Then, after substituting (27) and (28) into (29), the q-axis current during control satisfies the following condition

$$\begin{cases} i_q = \dfrac{-\sqrt{r} + \sqrt{-r + \frac{4T_l\psi_f}{3p(L_d - L_q)^2\sqrt{r}}}}{2} \\ r = \sqrt[3]{-\frac{q}{2} + \sqrt{\frac{q^2}{4} + \frac{p^2}{27}}} + \sqrt[3]{-\frac{q}{2} - \sqrt{\frac{q^2}{4} + \frac{p^2}{27}}} \\ p = \frac{16{T_l}^2}{9p^2(L_d - L_q)^2}, q = -\frac{4{T_l}^2{\psi_f}^2}{9p^2(L_d - L_q)^4} \end{cases}. \quad (30)$$

As for the PMM, the relation of motor currents and flux linkage is depicted in Fig. 7 under the rated load. In Fig. 7, the current magnitude i_s is square root of the sum of dq-axis current squares. Meanwhile, Fig. 7 quantitatively shows the current characteristics versus different demagnetization degrees. Because ψ_f is the overall PM flux linkage, it can be estimated by the AM in Section II

$$\psi_f = \begin{cases} 2p(1-\sigma)B_r l_{PM} l, & \text{if UD occurs} \\ (2p-\sigma)B_r l_{PM} l, & \text{if PD occurs} \end{cases}$$

$$i_{sf} = \begin{cases} i_s/(1-\sigma), & \text{if UD occurs} \\ i_s/(1-\sigma/2p), & \text{if PD occurs} \end{cases} \quad (31)$$

where i_{sf} is the current magnitude of demagnetized motors.

It is interesting that regardless of the UD and PD faults, both the dq-axis current magnitudes will increase once they appear, and the larger the demagnetization degree is, the higher the current magnitudes become. This is the main reason why the copper loss rises while the motor efficiency and torque output capacity drop when the demagnetization fault appears. As far as the current harmonics are concerned, they witness rare changes theoretically since the motional back EMF harmonics in Section II do not change significantly. However, in practice, the current magnitude variations might change the magnetic saturation property (with armature reaction considered) of the iron core. In this case, the current harmonics would shift but the changes are irregular.

The analysis presented in this section clearly shows that demagnetization faults significantly degrade the performance of PMMs driven by MTPA methods. However, the reduced performance, in turn, is inclined to exacerbate the degree of demagnetization, thereby setting a vicious cycle. These underscore the immense value of studying and implementing demagnetization suppression techniques prevent the fault from occurring or becoming more severe.

IV. Proposed MTPA-Driven Method Based on Loss Optimization to Suppress Demagnetization Fault

High temperature is an important cause of demagnetization faults in PMs. However, the demagnetization of a magnet is a gradual process [32], and some PM materials start to experience demagnetization even the temperature is 60 °C and the fault will get more severe during the long-time operations [33]. To suppress demagnetization fault caused by high temperature, this part introduces an improved MTPA strategy with an MPC controller integrated. As mentioned in [34], iron loss L_{iron} and copper loss L_{cu} are the primary losses in the PMM and have the most significant impact on motor temperature. Hence, the proposed MPC-based MTPA strategy not only takes into copper loss but also iron loss. It needs to be mentioned that the primary objective of the article is to reduce the temperature rise by optimizing the motor's loss that is closely related to the control strategy. In terms of mechanical loss and stray loss, which are hard to be optimized through control methods, they are not addressed. Through the proposed MTPA strategy, the demagnetization of the PMs can be suppressed, ensuring the continued reliability and efficiency of the motor system.

As shown in Fig. 8, the proposed MTPA method uses MPC controller to replace the traditional PI current controllers in the control structure. Because MPC can handle multiple objectives simultaneously, which can achieve the machine loss optimization to reduce the PM temperature so that to suppress the demagnetization fault. In practice, the mathematical model needs to be used to predict the future states for an FCS-MPCC strategy. After applying Euler discretization algorithm to (27), the DPM of PMMs in the direct-quadrature rotating frame can be described as

$$i_d(k+1) = \frac{L_d - TR_s}{L_d} i_d(k) + \frac{TL_q p}{L_d}\omega_m(k) i_q(k) + \frac{T}{L_d} u_d(k) \quad (32)$$

$$i_q(k+1) = -\frac{TL_d p}{L_q}\omega_m(k)i_d(k) + \frac{L_q - TR_s}{L_q}i_q(k) + \frac{T}{L_q}u_q(k) - \frac{T\Psi_f p}{L_q}\omega_m(k) \tag{33}$$

where T is control period.

To optimize motor losses more effectively, the motor losses are calculated based on the predicted current and given voltages. When ignoring the losses other than copper and iron losses. First, the future copper loss can be calculated by

$$L_{cu}(k+1) = \lambda m R_s \left(i_d^2(k+1) + i_q^2(k+1)\right) \tag{34}$$

where λ is transform coefficient. It's worth noting that $\lambda = 1.5$ when the motor coordinate system undergoes a fixed amplitude transformation, while it takes on a value of 1 when the system experiences a fixed power transformation. Second, the total iron loss L_{iron} can be predicted by

$$\begin{cases} L_{\text{iron}}(k+1) = L_{\text{all}}(k+1) - L_{\text{cu}}(k+1) \\ L_{\text{all}}(k+1) = \lambda(u_d i_d(k+1) + u_q i_q(k+1)) - \omega_m T_L \end{cases} \tag{35}$$

where L_{all} is the total motor loss. In (35), T_l can be calculated by using the observer in [35] instead of (29). The total iron loss L_{iron} contains both rotor iron loss and stator iron loss, which can be further calculated by

$$\begin{cases} L_{\text{iron}r}(k+1) = \gamma_1 L_{\text{iron}}(k+1) \\ L_{\text{iron}s}(k+1) = (1-\gamma_1) L_{\text{iron}}(k+1) \end{cases} \tag{36}$$

where $L_{\text{iron}r}$ is rotor iron loss, $L_{\text{iron}s}$ is stator iron loss, γ_1 is the proportion of $L_{\text{iron}r}$ to L_{iron}. Based on the FEM simulation results for the motor in this article, γ_1 is approximately 0.15.

After using (32) and (33) to calculate the future currents i_d $(k+1)$, i_q $(k+1)$ and the motor loss corresponding to different voltage vectors, they will be applied in the cost function (37) to choose the optimal control vector. The cost function J can be divided into two distinct cost functions: the electrical function J_e and the temperature function J_t

$$\begin{cases} J = k_1 J_e + k_2 J_t \\ J_e = |i_d^* - i_d(k+1)| + |i_q^* - i_q(k+1)| \\ J_t = \frac{L_{\text{iron}s}(k+1)}{d_1} + \frac{L_{\text{cu}}(k+1)}{d_2} + \frac{L_{\text{iron}r}(k+1)}{d_3} \end{cases} \tag{37}$$

where k_i is weight coefficient, $i_d^*$and i_q^* represent the reference currents, $1/d_i$ represent the extent to which the loss of each component affects the temperature of the PM approximately

$$d_i = \frac{R_i}{R_r} \tag{38}$$

where R_i is the distance between the i section that produces the loss to the motor axis, R_r is the outer radius of the motor rotor.

Before leaving this part, three aspects concerning the proposed MTPA method need to be addressed. First, being different from the analytical process and results in Section II, the proposed MTPA control method is not influenced by the value of SPP. This happens because (28), (30), and (32)–(38) demonstrate that the proposed MTPA strategy is only related the motor parameters (e.g., resistance, inductance, and flux linkage, etc.) and working states. Second, cost function (37) distinguishes itself from other model predictive control methodologies, such as the one detailed in [36], by its focused optimization on both electrical performance and loss reduction. This dual emphasis provides a distinct advantage in tackling the essential challenges associated with motor performance, loss, and temperature management. Third, similar to the multitarget cost function approach in [36], the proposed method introduces certain drawbacks, including the increased complexity involved in managing the tradeoffs between electrical and thermal performance metrics. Practically, the weight coefficients in (37) require empirical tuning.

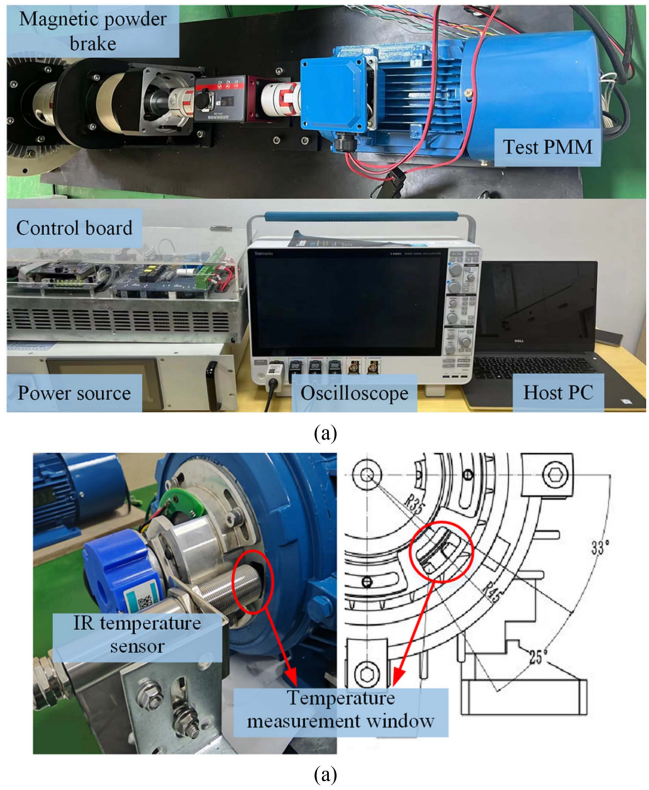

Fig. 9. Test bench used for verifications.

V. Verification Results

To verify the theoretical findings and the proposed MTPA method, simulations and physical experiments are conducted on the 24-slot/4-pole interior PMMs. The parameters of the healthy test motor are given in Table II. Besides, to simulate the condition of PM demagnetization, two motors are specially customized. In one motor, all PMs are magnetized to 90% of their rated value, representing a 10% UD fault, while in the other motor, one PM was not magnetized, signifying a 100% PD fault. The experimental setup is shown in Fig. 9. For the hardware platform, the test algorithms are executed on a DSP TMS320F 28335 control board. The control frequency of the proposed MTPA method is set as 10 kHz, which is high enough to suppress harmonics caused by the control strategy in this article. Data can be monitored by the control desk installed on the host

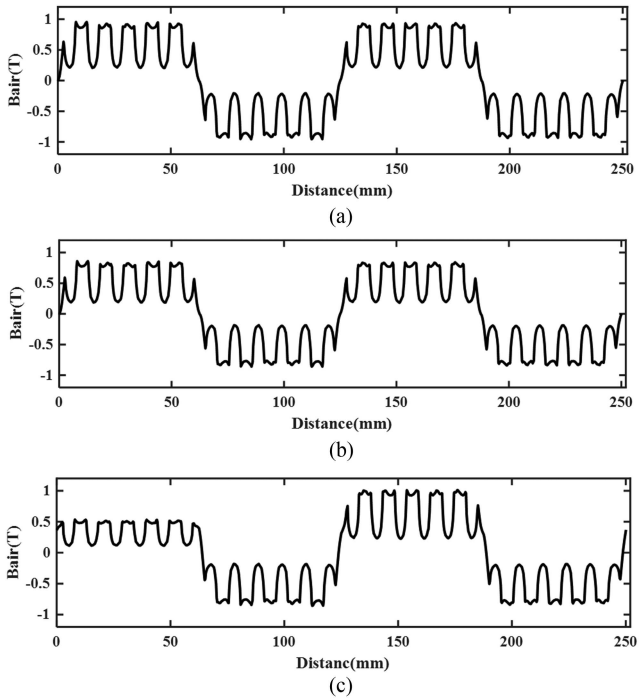

Fig. 10. Air gap flux density of different PMMs. (a) Healthy motor. (b) Motor under 10% UD fault. (c) Motor under 50% PD fault.

PC and recorded by an oscilloscope. One magnetic powder brake is connected to the test motor to provide the required load. It is worth mentioning that, to measure the temperature of the motor rotor, as shown in the Fig. 9(b), a measurement window is created on the motor's rear cover for rotor temperature measurement. An infrared sensor is positioned to measure the rotor's real-time temperature without making direct contact.

A. Validation of Fault Modeling and Demagnetization Fault Impact on Back EMF

Finite element simulation is first carried out to verify the proposed model and analytical results. The motor parameters are consistent with those in Table I. Back EMFs of the motor are given in this part, which can validate the results given in Sections III.

Fig. 10 shows the air gap flux density of the healthy machine and two fault machines without load. It can be noted that the peak value of the healthy air-gap flux density B_{air} is 0.93 T. In the case of a 50% PD fault, where one of the motor poles has lost half of its PM remanence, the air-gap flux density under the pole is 0.52 T. And the peak value of air-gap flux density under 10% UD fault is 0.84 T. As mentioned above, the magnetic field generated by the PMs inside the motor is trapezoidal, corroborating the assumption that the behavior of magnetic density is both reasonable and accurate. These results prove the accuracy of (9) and (10), validating the correctness of the AM. Hence, the AM can be treated as an effective method for subsequent back EMF analysis.

Then, the back EMFs of the three motors are tested experimentally to verify the proposed model and analytical results. During

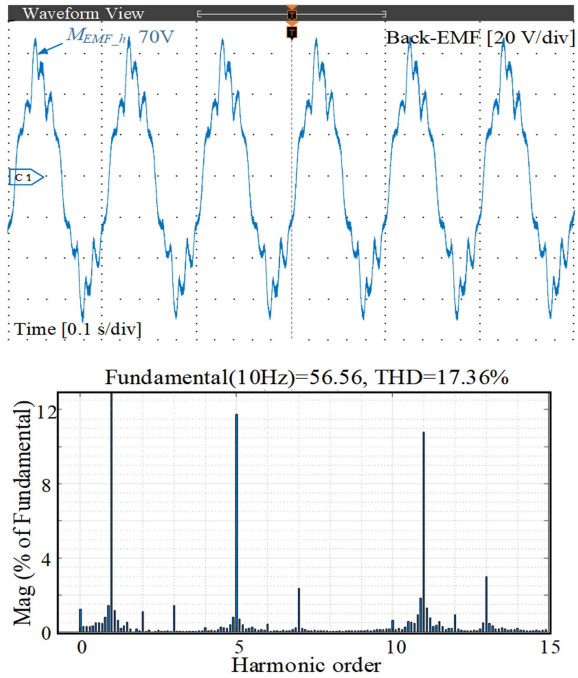

Fig. 11. *a*-phase motional back EMF of the healthy PMM.

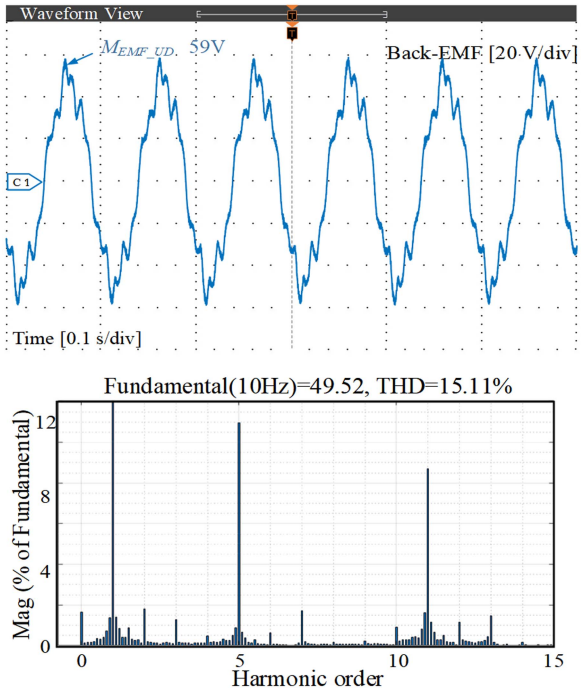

Fig. 12. *a*-phase motional back EMF of PMM: under 10% UD fault.

the experiment, a healthy motor working under 300 r/min is used to drive three test motors: a healthy PMM, a PMM with a 100% PD, and a PMM with a 10% UD. The back EMF waveforms for each motor are recorded. Figs. 11–13 and Table III compare the motional back EMF of the PMM prototypes. The *a*-phase fundamental back EMF of the healthy machine measures 56.6 V. Meanwhile, the back EMF under 100% PD fault and 10% UD

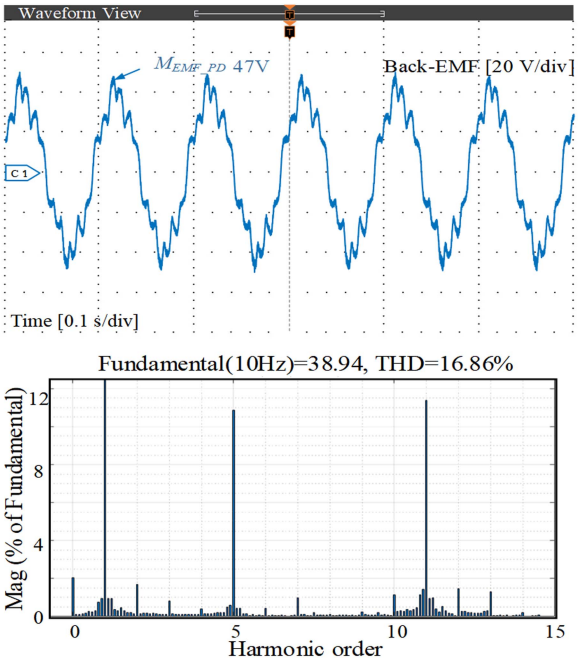

Fig. 13. a-phase motional B-EMF of the PMM under 100% PD fault.

TABLE III
BACK EMFS OF THREE MOTORS UNDER DIFFERENT DEMAGNETIZATION FAULT

Motors	Overall back EMFs (V)	Fundamental back EMFs (V)	THD (%)
Healthy motor	70	56.56	17.36
Motor under 10% UD fault	59	49.52	15.11
Motor under 50% PD fault	47	38.94	16.86

fault respectively is 38.9 and 49.5 V, representing reductions of 31.2% and 12.5% from the standard back EMF value. There is a slight deviation between the analytical results and the experimental results, and the reasons for this phenomenon are twofold. First, there is an error in magnetizing the pole in the faulty motor. Second, the demagnetization of a single pole affects the other poles of the motor, leading to a reduction in the overall magnetic flux density.

In terms of the back EMF harmonics, the values of THD for the healthy motor, motor under 10% UD, and motor under 100% PD are 17.36%, 15.11%, and 16.86%, respectively. They see very small differences, complying with the analytical results shown in Section II. Interestingly, by carefully comparing the back EMFs in Figs. 11, 12, and 13, their phases see similar trend as well.

Overall, both the FEM and experimental results prove that the proposed AM and analytical results are effective, and meanwhile, it is reasonable to ignore the magnetic saturation during the modeling process. Besides, what needs to be addressed is that, first, unlike the AMs based on magnetic equivalent circuit theory referenced in [17] and [18], the proposed AM does not require complex mathematical calculations. Instead, it can equally demonstrate the overall properties of the PMMs under

TABLE IV
CURRENTS OF THREE MTPA-DRIVEN MOTORS UNDER DIFFERENT DEMAGNETIZATION FAULT

Motors	i_s (A)	i_q (A)	i_d (A)
Healthy motor	2.06	2.05	-0.21
Motor under 10% UD fault	2.35	2.28	-0.33
Motor under 50% PD fault	2.88	2.83	-0.52

demagnetization faults. Second, in contrast to the AM developed to analyze a single conductor in [23], which indicates that the back EMF waveform of a single conductor aligns with the asymmetrical air-gap magnetic field's waveform, the proposed method shows that the overall back EMF within the windings is symmetrical. This distinction is a significant contribution of this research, facilitating a more straightforward understanding of the features of the demagnetization faults.

B. Impacts of Demagnetization Fault Impacts on Currents

To validate the quantitative analysis of the impact of demagnetization on the currents of MTPA-driven PMMs, experiment is conducted on the healthy motor. The goal is to corroborate the theoretical findings and assess the practical effects of demagnetization faults on motor performance. In this part, the results of phase currents that contain the amplitude and harmonic information are provided. For the sake of comprehensiveness, the impacts of demagnetization on phase current, overall current amplitude, and dq-axis current amplitude are provided.

Fig. 14 illustrates the performance of dq-axis currents and a-phase current (i_a) when the three tested motors work at 600 r/min under 4 N·m. It also shows how current characteristics change with different demagnetization faults.

In Fig. 14(a), the current characteristics are all normal. i_d and i_q are -0.21 and 2.05 A. The overall current magnitude i_s is 2.06 A. The amplitude of a-phase current is 2.10 A. In Fig. 14(b), the current characteristics for PMM under 10% UD exhibit minor variations. i_d and i_q are -0.33 A and 2.28 A. i_s is 2.35 A. And the amplitude of i_a is 2.38 A, has increased by 13.3%. In Fig. 14(c), the current characteristics under 50% PD have significant changes. i_d and i_q are -0.52 A and 2.83 A. i_s is 2.88 A. And the amplitude of i_a is 2.91 A, has increased by 38.1%. Table IV gives the current performance, and it can be noted that the current variation trends comply with the analytical results in Section III-B.

Notably, regardless of the UD and PD faults, the magnitudes of motor currents increase with the severity of demagnetization. This increase is a key reason for the rise in copper losses, as well as the reduction in motor efficiency and torque output capacity. The results in this section clearly demonstrate that the demagnetization faults have a significant and adverse impact on the motor performance. The experimental results align with the theoretical analysis, confirming the significance of addressing demagnetization in practice. By contrast with the previous studies such as [22], [23], [24], [25], [26], [27], which did not address the quantitative impacts of demagnetization faults on

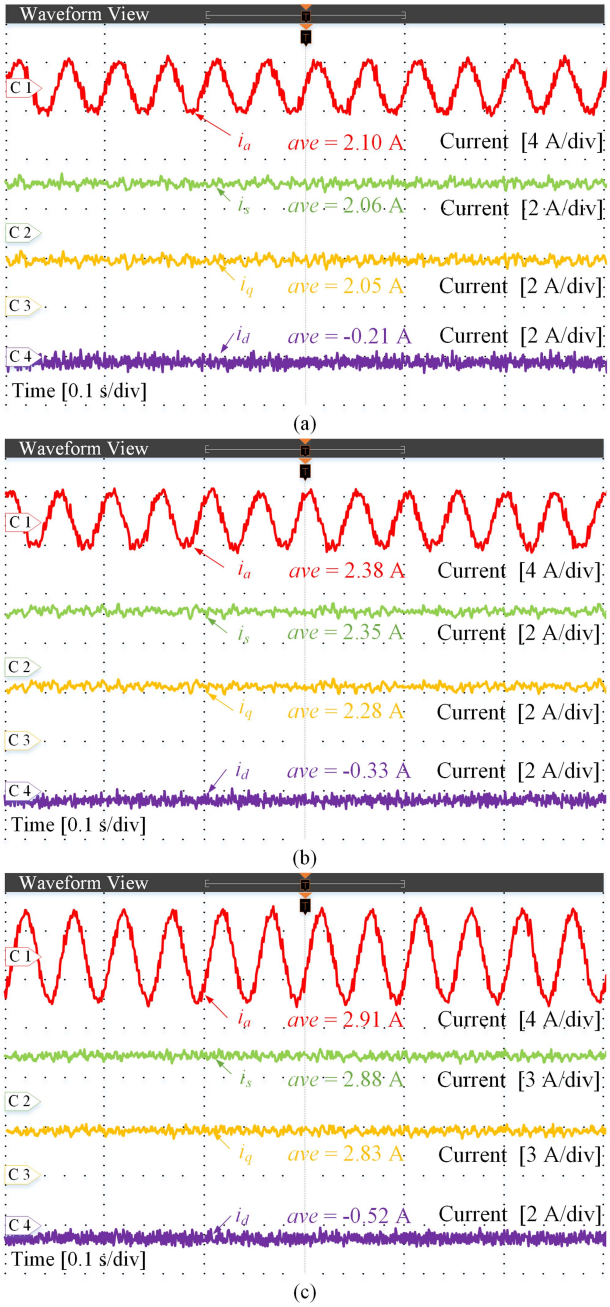

Fig. 14. Comparative results of different PMMs at 600 r/min with 4 Nm load. (a) Healthy motor. (b) Motor under under 10% UD fault. (c) Motor under 100% PD fault.

the control performance, the aforesaid analytical results clearly show that the current changes are quantitatively related to the demagnetization severity. Hopefully, the analytical results together with the experimental results in this research will serve as basic principles to explain the performance of a specific motor once it experiences the fault.

C. Validation of the Proposed Demagnetization Suppression Strategy

To validate the proposed MTPA algorithm, it is used to control the test motor to operate in a 25 °C environment for 2 h. Electrical

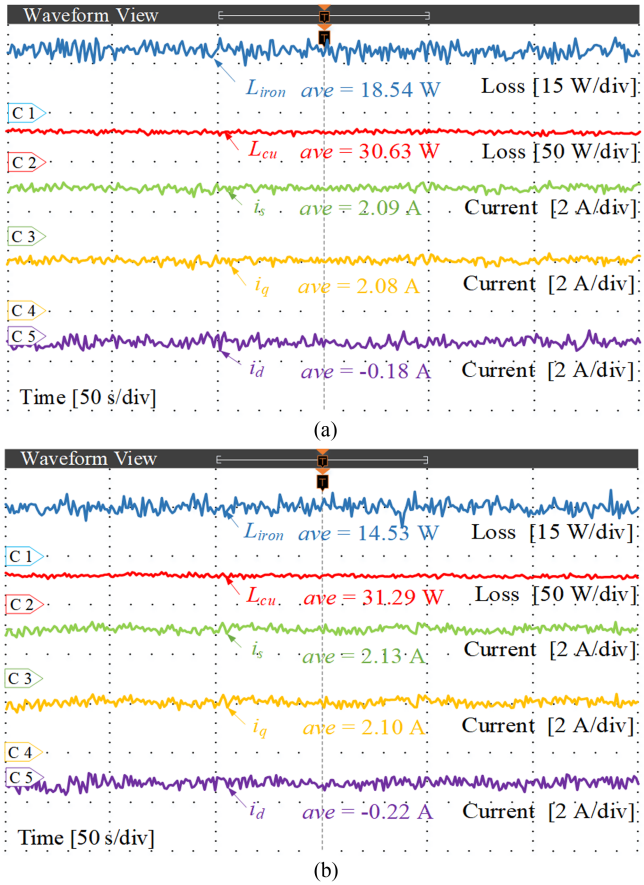

Fig. 15. Comparative results of different control strategies under condition 1. (a) Performance of traditional MTPA algorithms. (b) Performance of proposed MTPA strategy.

signals and temperature data were collected under four different operating conditions. To well balance the performance of current and losses, the weight coefficient k_1 and k_2 set as 1 and 0.0025 through empirical methods.

1) *Condition* 1: The motor rotates at 600 r/min with a torque of 4 N·m.
2) *Condition* 2: The motor rotates at 600 r/min with a torque of 2 N·m.
3) *Condition* 3: The motor rotates at 400 r/min with a torque of 4 N·m.
4) *Condition* 4: The motor rotates at 400 r/min with a torque of 2 N·m.

For the purpose of comparison, the performance of the traditional MTPA strategy will also be given to show the advantages of the proposed methods. Considering that the proposed MTPA method aims to reduce temperature rise by optimizing copper and iron losses, the results related to temperature and losses are presented to demonstrate the superiority of the new method. Additionally, recognizing that current characteristics are key factors influencing losses, the overall current amplitude along with the constituent *dq*-axis current information is also provided for comparison purposes.

1) Condition 1: Fig. 15(a) denotes the performance of the traditional MTPA method when motor speed is 600 r/min under

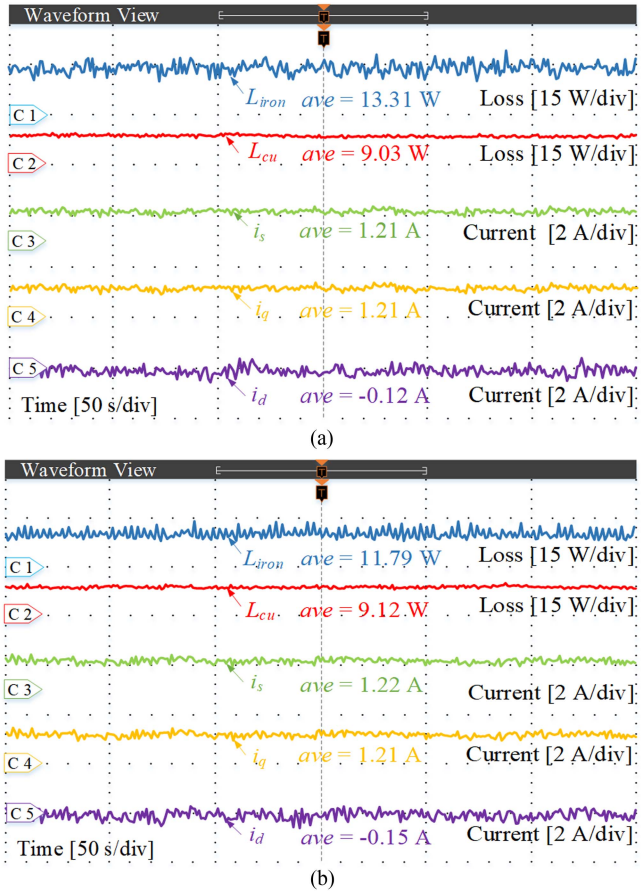

Fig. 16. Comparative results of different control strategies under condition 2. (a) Performance of traditional MTPA algorithms. (b) Performance of proposed MTPA strategy.

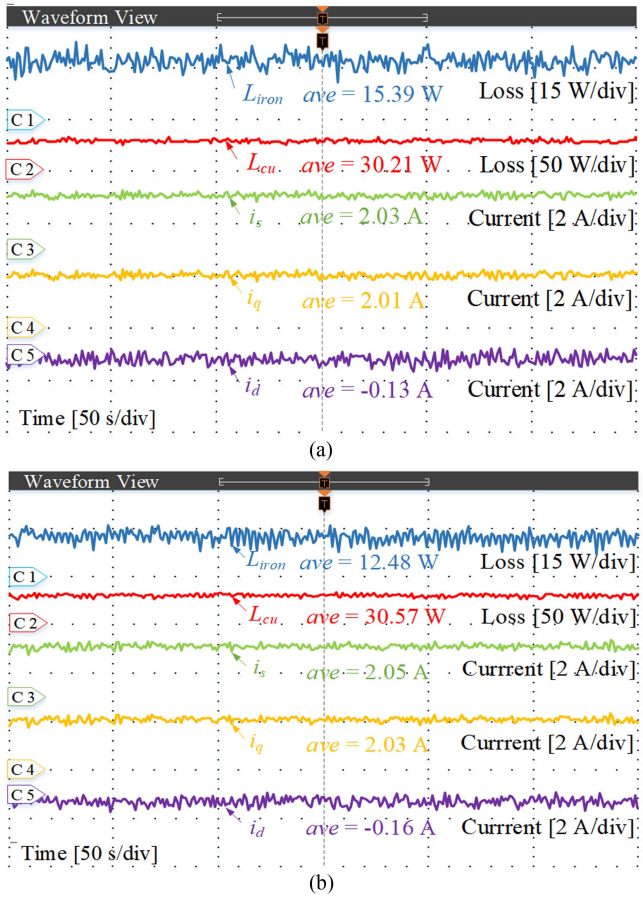

Fig. 17. Comparative results of different control strategies under condition 3. (a) Performance of traditional MTPA algorithms. (b) Performance of proposed MTPA strategy.

4 N·m in 5 min. i_d and i_q are −0.18 and 2.08 A. The current magnitude i_s is 2.09 A. In addition, the copper loss L_{cu} of the machine is 30.63W and the iron loss L_{iron} is 18.54 W. Fig. 15(b) denotes the performance of the proposed MTPA method. i_d and i_q are −0.22 and 2.10 A. The current magnitude i_s is 2.12 A. In addition, the copper loss L_{cu} of the machine is 31.29 W and the iron loss L_{iron} is 14.53 W. From the above results, compared to the traditional control method, it can be observed that the current values of the proposed algorithm have a 1.1% increase. Notably, while the copper losses have slightly rises by 2.1%, there has been a significant reduction in iron losses, amounting to 21.5%. This demonstrates that the proposed algorithm maintains comparable electrical efficiency to the traditional method, yet achieves a notable decrease in overall losses.

2) Condition 2: Fig. 16(a) denotes the performance of the traditional MTPA method when motor speed is 600 r/min under 4 N·m in 5 min. i_d and i_q are −0.12 and 1.21 A, respectively. The current magnitude i_s is 1.21 A. In addition, the copper loss L_{cu} of the machine is 9.03 W and the iron loss L_{iron} is 13.31 W. Fig. 16(b) denotes the performance of the proposed MTPA method. i_d and i_q are −0.15 and 1.21 A, respectively. The current magnitude i_s is 1.22 A. In addition, the copper loss L_{cu} of the machine is 9.12 W and the iron loss L_{iron} is 11.79 W. From the above results, compared to the traditional method, it can be observed that the overall current values of the proposed algorithm have a 1.0% increase. The copper loss increases by 1.0%, but the iron loss decreases by 11.5%.

3) Condition 3: Fig. 17(a) denotes the performance of the traditional MTPA method when motor speed is 600 r/min under 4 N·m in 5 min. i_d and i_q are −0.13 and 2.01 A, respectively. The current magnitude i_s is 2.03 A. In addition, the copper loss L_{cu} of the machine is 30.21 W and the iron loss L_{iron} is 15.39 W. Fig. 17(b) denotes the performance of the proposed MTPA method. i_d and i_q are −0.16 and 2.03 A, respectively. The current magnitude i_s is 2.05 A. In addition, the copper loss L_{cu} of the machine is 30.57 W and the iron loss L_{iron} is 12.48 W. From the above results, it can be observed that the current values of the proposed algorithm are largely consistent with those calculated using the traditional MTPA algorithm, with a 1.0% increase. The copper loss increases by 1.2%, but the iron loss decreases by 18.8%.

4) Condition 4: Fig. 18(a) denotes the performance of the traditional MTPA method when motor speed is 600 r/min under 4 N·m in 5 min. i_d and i_q are −0.08 and 1.14 A, respectively. The current magnitude i_s is 1.14 A. In addition, the copper loss L_{cu} of the machine is 8.22 W and the iron loss L_{iron} is 12.15 W. Fig. 18(b) denotes the performance of the proposed MTPA method. i_d and i_q are −0.12 and 1.15 A, respectively. The

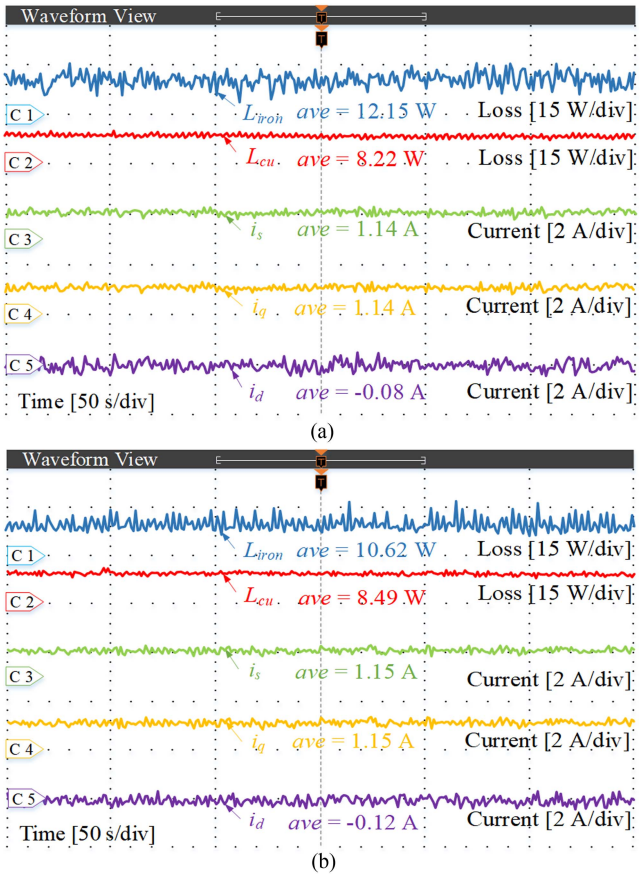

Fig. 18. Comparative results of different control strategies under condition 4. (a) Performance of traditional MTPA algorithms. (b) Performance of proposed MTPA strategy.

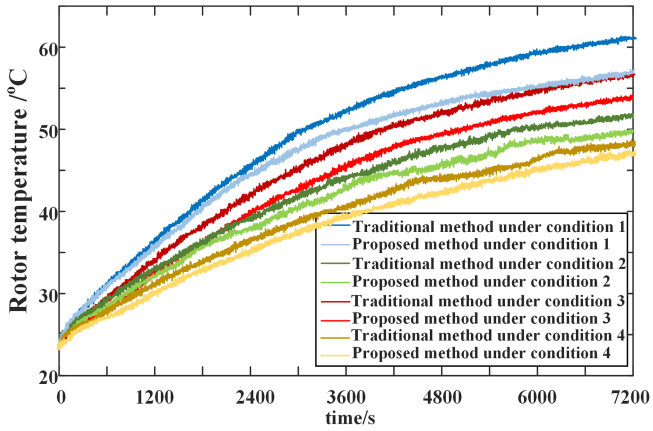

Fig. 19. Temperature of PMs under different working conditions.

TABLE V
IRON AND COPPER LOSSES UNDER DIFFERENT CONDITIONS

Conditions	Traditional MTPA			Proposed MTPA		
	L_{iron} (W)	L_{cu} (W)	Overall (W)	L_{iron} (W)	L_{cu} (W)	Overall (W)
Condition 1	18.54	30.63	49.17	14.53	31.29	45.82
Condition 2	13.31	9.03	22.34	11.79	9.12	20.91
Condition 3	15.39	30.21	45.60	12.48	30.57	43.05
Condition 4	12.15	8.22	20.37	10.62	8.49	19.11

TABLE VI
MOTOR TEMPERATURE RISE UNDER DIFFERENT WORKING CONDITIONS

Method	Condition 1	Condition 2	Condition 3	Condition 4
Traditional method	66.6°C	57.2°C	61.7°C	53.4°C
Proposed method	61.5°C	54.6°C	57.7°C	50.2°C

current magnitude i_s is 1.15 A. In addition, the copper loss L_{cu} of the machine is 8.49 W and the iron loss L_{iron} is 10.62 W. It can be noted that the electrical performance of the proposed algorithm closely aligns with that of the traditional MTPA algorithm, with only a minor increase of 0.9% in current values. The copper losses have increased by 3.3%, but iron losses have decreased by 12.6%.

Furthermore, as shown in Fig. 19, after two hours of operation, the rotor temperatures for both the traditional algorithm and the proposed algorithm are as follows: 62.3 °C and 57.4 °C in condition 1; 52.8 °C and 51.0 °C in condition 2; 57.7 °C and 54.8 °C in condition 3; 48.1 °C and 47.3 °C in condition 4.

After continuously operating for five hours, the temperature rise of the motor in different operating conditions has stabilized, and the final temperature values under different conditions are given in Table VI. Overall, the proposed MTPA algorithm consistently results in a lower rotor temperature rise compared to the traditional MTPA algorithm, regardless of working conditions. This phenomenon occurs because the proposed MTPA control method can reduce the overall losses, as given in Table V. It can be concluded that the PMs in motors controlled by the proposed MTPA method are subjected to lower risks of demagnetization because they experience lower temperature rises. Compared to the techniques in [28], [29], and [30], the proposed method is dedicated to suppressing demagnetization faults by refining control strategies. The superiority of the proposed MTPA method is evident because of the broader applicability.

Interestingly, the temperature rises in Fig. 19 are not high, which happens because the motor prototype used in this article has low rated load and low rated speed. This does not mean the proposed method cannot be used in the motors experiencing high temperature rises. Theoretically, the proposed MTPA strategy is able to suppress demagnetization faults by reducing temperature rises of any motors. It should be noted that the temperature increases depicted in Fig. 19 and Table VI are attributed not only to the losses in copper and iron but also to mechanical losses. Nevertheless, the experimental results demonstrate that the temperature rise of the motor is significantly reduced when the proposed MTPA method, which considers only copper and iron losses, is applied for control. This indicates that optimizing a subset of losses (excluding mechanical loss and stray loss) can effectively mitigate temperature increase and demagnetization.

This constitutes a major advantage of the proposed MTPA strategy.

VI. Conclusion

This article contributes to the understanding and suppression of demagnetization faults in MTPA-driven PMMs with distributed windings. First, an innovative structural-mathematical technique is introduced for modeling, which provides a more accurate representation of motor behavior under demagnetization faults. Second, the detailed quantitative analysis of demagnetization's impact on the back EMF and currents of the MTPA-driven PMMs enhances our understanding of the characteristics of the demagnetization fault, addressing the necessity of developing fault suppression strategies. Third, a new loss optimization-based MTPA strategy is proposed to suppress demagnetization fault caused by temperature rise, offering an approach to mitigate demagnetization risks in practical applications. Finally, the proposed AM, analytical results, and fault suppression strategy are validated by experiment. Overall, by addressing the challenges in PMM demagnetization research, this article provides valuable insights for improving the performance and reliability of the motors.

References

[1] J. Gao, W. Gui, C. Yang, T. Peng, J. Luo, and C. Yang, "Demagnetization modeling and analysis for MTPA-driven permanent magnet motors with distributed lap windings," in *Proc. IEEE Appl. Power Electron. Conf. Expo.*, 2023, pp. 1352–1357.

[2] C. Gong, Y. Hu, J. Gao, Y. Wang, and L. Yan, "An improved delay-suppressed sliding-mode observer for sensorless vector-controlled PMSM," *IEEE Trans. Ind. Electron.*, vol. 67, no. 7, pp. 5913–5923, Jul. 2020.

[3] C. Gong et al., "Hybrid DC-bus capacitor discharge strategy using internal windings and external bleeder for surface-mounted PMSM-based EV powertrains in emergency," *IEEE Trans. Ind. Electron.*, vol. 68, no. 3, pp. 1905–1915, Mar. 2021.

[4] X. Zhao and S. Niu, "A new slot-PM vernier reluctance machine with enhanced zero-sequence current excitation for electric vehicle propulsion," *IEEE Trans. Ind. Electron.*, vol. 67, no. 5, pp. 3528–3539, May 2020.

[5] M. Zhu, B. Yang, W. Hu, G. Feng, and N. C. Kar, "Vold-Kalman filtering order tracking based rotor demagnetization detection in PMSM," *IEEE Trans. Ind. Appl.*, vol. 55, no. 6, pp. 5768–5778, Nov./Dec. 2019.

[6] J. Faiz and H. Nejadi-Koti, "Demagnetization fault indexes in permanent magnet synchronous motors—An overview," *IEEE Trans. Magn.*, vol. 52, no. 4, Apr. 2016, Art. no. 8201511.

[7] S. Choi et al., "Fault diagnosis techniques for permanent magnet AC machine and drives—A review of current state of the art," *IEEE Trans. Transp. Electrific.*, vol. 4, no. 2, pp. 444–463, Jun. 2018.

[8] S. Zhu, M. Cheng, W. Hua, X. Cai, and M. Tong, "Finite element analysis of flux-switching PM machine considering oversaturation and irreversible demagnetization," *IEEE Trans. Magn.*, vol. 51, no. 11, Nov. 2015, Art. no. 7403404.

[9] S. G. Lee, K.-S. Kim, J. Lee, and W. H. Kim, "A novel methodology for the demagnetization analysis of surface permanent magnet synchronous motors," *IEEE Trans. Magn.*, vol. 52, no. 3, Mar. 2016, Art. no. 7003404.

[10] W. N. Fu and S. L. Ho, "Dynamic demagnetization computation of permanent magnet motors using finite element method with normal magnetization curves," *IEEE Trans. Appl. Supercond.*, vol. 20, no. 3, pp. 851–855, Jun. 2010.

[11] J. A. Farooq, A. Djerdir, and A. Miraoui, "Analytical modeling approach to detect magnet defects in permanent-magnet brushless motors," *IEEE Trans. Magn.*, vol. 44, no. 12, pp. 4599–4604, Dec. 2008.

[12] J. Lee, Y.-J. Jeon, D.-C. Choi, S. H. Kim, and S. W. Kim, "Demagnetization fault diagnosis method for PMSM of electric vehicle," in *Proc. 39th Annu. Conf. IEEE Ind. Electron. Soc.*, 2013, pp. 2709–2713.

[13] C. Zhang et al., "Robust fault-tolerant predictive current control for permanent magnet synchronous motors considering demagnetization fault," *IEEE Trans. Ind. Electron.*, vol. 65, no. 7, pp. 5324–5334, Jul. 2018.

[14] J. De Bisschop, A. Abdallh, P. Sergeant, and L. Dupré, "Identification of demagnetization faults in axial flux permanent magnet synchronous machines using an inverse problem coupled with an analytical model," *IEEE Trans. Magn.*, vol. 50, no. 11, Nov. 2014, Art. no. 8104804.

[15] S. Chakraborty et al., "Detection and estimation of demagnetization faults in permanent magnet synchronous motors," *Elect. Power Syst. Res.*, vol. 96, pp. 225–236, Mar. 2013.

[16] S. S. Moosavi, A. Djerdir, Y. A. Amirat, and D. A. Khaburi, "Demagnetization fault diagnosis in permanent magnet synchronous motors: A review of the state-of-the-art," *J. Magnetism Magn. Mater.*, vol. 391, pp. 203–212, 2015.

[17] W. Gui, J. Gao, C. Yang, T. Peng, C. Yang, and Y. Han, "Optimized FCS-MPCC based on disturbance feedback rejection for IPMSMs under demagnetization fault in high-speed trains," *Control Eng. Pract.*, vol. 141, Dec. 2023, Art. no. 105670.

[18] W. Wang, X. Liu, D. Liu, and S. Zhu, "Design and analysis of a novel flux-intensifying flux-controlled permanent magnet motor," in *Proc. IEEE 5th Int. Elect. Energy Conf.*, 2022, pp. 2355–2359.

[19] A. Usman, B. M. Joshi, and B. S. Rajpurohit, "Modeling and analysis of demagnetization faults in BLDC motor using hybrid analytical-numerical approach," in *Proc. IEEE 45th Annu. Conf. Ind. Electron. Soc.*, 2019, pp. 1198–1203.

[20] T. Raminosoa, J. A. Farooq, A. Djerdir, and A. Miraoui, "Reluctance network modelling of surface permanent magnet motor considering iron nonlinearities," *Energy Convers. Manage.*, vol. 50, no. 5, pp. 1356–1361, 2009.

[21] J. Faiz and E. Mazaheri-Tehrani, "Demagnetization modeling and fault diagnosing techniques in permanent magnet machines under stationary and nonstationary conditions: An overview," *IEEE Trans. Ind. Appl.*, vol. 53, no. 3, pp. 2772–2785, May/Jun. 2017.

[22] A. G. Espinosa, J. A. Rosero, J. Cusidó, L. Romeral, and J. A. Ortega, "Fault detection by means of Hilbert–Huang transform of the stator current in a PMSM with demagnetization," *IEEE Trans. Energy Convers.*, vol. 25, no. 2, pp. 312–318, Jun. 2010.

[23] J.-C. Urresty, J.-R. Riba, M. Delgado, and L. Romeral, "Detection of demagnetization faults in surface-mounted permanent magnet synchronous motors by means of the zero-sequence voltage component," *IEEE Trans. Energy Convers.*, vol. 27, no. 1, pp. 42–51, Mar. 2012.

[24] M. Zhu, W. Hu, and N. C. Kar, "Acoustic noise-based uniform permanent-magnet demagnetization detection in SPMSM for high-performance PMSM drive," *IEEE Trans. Transp. Electrific.*, vol. 4, no. 1, pp. 303–313, Mar. 2018.

[25] M. Zhu, W. Hu, and N. C. Kar, "Torque-ripple-based interior permanent-magnet synchronous machine rotor demagnetization fault detection and current regulation," *IEEE Trans. Ind. Appl.*, vol. 53, no. 3, pp. 2795–2804, May/Jun. 2017.

[26] M. Zafarani, T. Goktas, and B. Akin, "A comprehensive magnet defect fault analysis of permanent-magnet synchronous motors," *IEEE Trans. Ind. Appl.*, vol. 52, no. 2, pp. 1331–1339, Mar./Apr. 2016.

[27] A. Usman, V. K. Sharma, and B. Singh Rajpurohit, "Harmonic analysis of a BLDC motor under demagnetization fault conditions," in *Proc. IEEE 9th Power India Int. Conf.*, 2020, pp. 1–5.

[28] J.-W. Jung, B.-H. Lee, K.-S. Kim, and J.-P. Hong, "Design of IPMSM for reduction of eddy current loss in permanent magnets to prevent irreversible demagnetization," in *Proc. IEEE Int. Elect. Machines Drives Conf.*, 2017, pp. 1–6.

[29] O. Farrok, M. R. Islam, M. R. Islam Sheikh, Y. Guo, J. Zhu, and G. Lei, "Oceanic wave energy conversion by a novel permanent magnet linear generator capable of preventing demagnetization," *IEEE Trans. Ind. Appl.*, vol. 54, no. 6, pp. 6005–6014, Nov./Dec. 2018.

[30] K.-Y. Hwang and K.-Y. Yoon, "Fault-tolerant design process of spoke-type IPM motor considering irreversible demagnetization of PM in integrated electric brake system," *IEEE Trans. Magn.*, vol. 58, no. 11, Nov. 2022, Art. no. 8206809.

[31] G. T. de Paula, J. R. B. de A. Monteiro, T. E. P. de Almeida, M. P. de Santana, W. C. A. Pereira, and C. M. R. Oliveira, "Evaluation of surface mounted PM machine's parameters on load conditions using frozen permeability method. Part. II," in *Proc. IEEE 21st Int. Conf. Elect. Machines*, 2014, pp. 156–161.

[32] M.-D. Calin and E. Helerea, "Temperature influence on magnetic characteristics of NdFeB permanent magnets," in *Proc. 7th Int. Symp. Adv. Topics Elect. Eng.*, 2011, pp. 1–6.

[33] M. Haavisto, H. Kankaanpää, and M. Paju, "Estimation of time-dependent polarization losses in sintered Nd-Fe-B permanent magnets," *IEEE Trans. Magn.*, vol. 47, no. 1, pp. 170–174, Jan. 2011.
[34] O. Wallscheid and J. Böcker, "Global identification of a low-order lumped-parameter thermal network for permanent magnet synchronous motors," *IEEE Trans. Energy Convers.*, vol. 31, no. 1, pp. 354–365, Mar. 2016.
[35] C. Gong, Y. Hu, K. Ni, J. Liu, and J. Gao, "SM load torque observer-based FCS-MPDSC with single prediction horizon for high dynamics of surface-mounted PMSM," *IEEE Trans. Power Electron.*, vol. 35, no. 1, pp. 20–24, Jan. 2020.
[36] Y. Han, C. Gong, L. Yan, H. Wen, Y. Wang, and K. Shen, "Multiobjective finite control set model predictive control using novel delay compensation technique for PMSM," *IEEE Trans. Power Electron.*, vol. 35, no. 10, pp. 11193–11204, Oct. 2020.

Jinqiu Gao was born in Shannxi province in P.R. China, in 1996. She received the B.Eng. and M.Eng. degrees in electrical engineering from Northwestern Polytechnical University, Xi'an, China, in 2017 and 2020, respectively. She is currently working toward the Ph.D. degree in control science and engineering with the School of Automation, Central South University, Changsha, China.

Her research interests include electrical machines drives and motor fault diagnosis.

Weihua Gui (Member, IEEE) received the B.Eng. degree in electrical engineering and the M.Eng. degree in automatic control engineering from Central South University, Changsha, China, in 1976 and 1981, respectively.

From 1986 to 1988, he was a Visiting Scholar with the University Duisburg-Essen, Duisburg, Germany. From 1991 to 2018, he was a Full Professor with the School of Automation, Central South University. Since 2019, he has been a Full Professor with the School of Automation, Central South University. Since 2013, he has been an Academician of Chinese Academy of Engineering. His main research interests include the modeling and optimal control of complex industrial processes, fault diagnoses and distributed robust control.

Chao Yang (Member, IEEE) received the B.S. degree in automatic control from the Chongqing University of Science and Technology, Chongqing, China, in 2014, the M.Eng. degree in control engineering and the Ph.D. degree in control science and control engineering from Central South University, Changsha, China, in 2017 and 2021, respectively.

From 2012 to 2013, he was an Exchange Student with the National Central University, Taoyuan, Taiwan. From 2019 to 2021, he was a Visiting Doctoral Student with the University Duisburg-Essen, Duisburg, Germany. He is currently a Lecture with the School of Automation, Central South University. His research interests include fault diagnosis and healthy monitoring of traction control systems.

Tao Peng (Member, IEEE) received the M.S. degree in control science and engineering from the National University of Defense Technology, Changsha, China, in 1991, and the Ph.D. degree in control science and engineering from the Central South University, Changsha, China, in 2005.

From 2002 to 2003, she was a Visiting Scholar with the University Duisburg-Essen, Duisburg, Germany. From 2004 to 2010, she was a Full Professor with the School of Automation, Hunan University of Technology. Since 2010, she has been a Full Professor with the School of Information Science and Engineering, Central South University, Changsha, China.

Her research interests include fault diagnosis and fault-tolerant control for complex systems.

Yun Yang (Senior Member, IEEE) received B.Sc. degree in electrical engineering from Wuhan University, Wuhan, China, in 2012 and the Ph.D. degree in electrical engineering from the University of Hong Kong, Hong Kong, in 2017. He was a Research Assistant Professor with the Department of Electrical Engineering, The Hong Kong Polytechnic University. He is currently an Assistant Professor with the School of Electrical and Electronic Engineering, Nanyang Technological University. His research interests include wireless power transfer, renewable energy technologies, electric vehicles, power electronics, and advanced control.

Junze Luo was born in Hunan province in P.R. China, in 1999. He received the B.Eng. degree in automation in 2021 from Central South University, Changsha, China, where he is currently working toward the Master degree in control science and engineering with the School of Automation.

His research interests include motor temperature estimation and reliability evaluation.

Chunhua Yang (Fellow, IEEE) received the M.Eng. degree in automatic control engineering and the Ph.D. degree in control science and engineering from Central South University, Changsha, China, in 1988 and 2002, respectively.

She was with the Department of Electrical Engineering, Katholieke Universiteit Leuven, Leuven, Belgium, from 1999 to 2001. She is currently a Full Professor with Central South University, Changsha, China. Her current research interests include modeling and optimal control of complex industrial processes, intelligent control systems, and fault-tolerant computing of real-time systems.